Properties of dentin, enamel and their junction, studied with Brillouin scattering and compared to Raman microscopy

Alban Desoutter, Didier Felbacq, Csilla Gergely, Béla Varga, Laurent Bonnet, Pascal Etienne, Rémy Vialla, Frédéric Cuisinier, Hamideh Salehi, Emmanuel Rousseau, et al.

Version of Record: https://www.sciencedirect.com/science/article/pii/S0003996923001218
Manuscript_22c252fec899311d1287c3466f997ec1

Properties of dentin, enamel and their junction, studied with Brillouin scattering and compared to Raman microscopy

Alban Desoutter[1], Didier Felbacq[2], Csilla Gergely[2], Béla Varga[2], Laurent Bonnet[2], Pascal Etienne[2], Remy Vialla[2], Frédéric Cuisinier[1], Hamideh Salehi[1], Emmanuel Rousseau[2], Benoit Rufflé[2]

1 LBN, Univ. Montpellier, Montpellier, France

2 L2C, Univ. Montpellier, CNRS, Montpellier, France

Alban Desoutter: LBN, Univ. Montpellier, 545 avenue Professeur Jean-Louis Viala, 34193 Montpellier Cedex 5. Mail: alban.desoutter@umontpellier.fr

Didier Felbacq: L2C, Univ. Montpellier, CNRS, place Eugène Bataillon, 34090 Montpellier, France. Mail: didier.felbacq@umontpellier.fr

Csilla Gergely: L2C, Univ. Montpellier, CNRS, place Eugène Bataillon, 34090 Montpellier, France. Mail: csilla.gergely@umontpellier.fr

Béla Varga: L2C, Univ. Montpellier, CNRS, place Eugène Bataillon, 34090 Montpellier, France. Mail: beduska@yahoo.co.uk

Laurent Bonnet: L2C, Univ. Montpellier, CNRS, place Eugène Bataillon, 34090 Montpellier, France. Mail: laurent.bonnet@umontpellier.fr

Pascal Etienne: L2C, Univ. Montpellier, CNRS, place Eugène Bataillon, 34090 Montpellier, France. Mail: pascal.etienne@umontpellier.fr

Remy Vialla: L2C, Univ. Montpellier, CNRS, place Eugène Bataillon, 34090 Montpellier, France. Mail: remy.vialla@umontpellier.fr

Frédéric Cuisinier: LBN, Univ. Montpellier, 545 avenue Professeur Jean-Louis Viala, 34193 Montpellier Cedex 5. Mail: frederic.cuisinier@umontpellier.fr

Hamideh Salehi: LBN, Univ. Montpellier, 545 avenue Professeur Jean-Louis Viala, 34193 Montpellier Cedex 5. Mail: s_hamideh@yahoo.com

Emmanuel Rousseau: L2C, Univ. Montpellier, CNRS, place Eugène Bataillon, Montpellier, 34090 France. Mail: emmanuel.rousseau@umontpellier.fr

Benoit Rufflé: L2C, Univ. Montpellier, CNRS, place Eugène Bataillon, 34090 Montpellier, France. Mail: benoit.ruffle@umontpellier.fr

Corresponding author:
Alban Desoutter, LBN, Univ. Montpellier, 545 avenue professeur Jean-Louis Viala, 34193 Montpellier Cedex 5. Mail: alban.desoutter@umontpellier.fr

Abstract

Objective

Dentin, enamel and the transition zone, called the dentin-enamel junction (DEJ), **have** an organization and properties that play a critical role in tooth resilience and in stopping the propagation of cracks. Understanding **their** chemical and micro-biomechanical properties is then of **foremost** importance. **The aim of this study is to apply Brillouin microscopy on a complex biological structure, that is, the DEJ, and to compare these results with those obtained with Raman microscopy.**

Design

Both techniques allow **noncontact** measurements at the microscopic scale. Brillouin microscopy **is** based on **the** interaction between acoustic phonons and laser photons and gives a relation between the frequency shift of the scattered light and **the** stiffness of the sample. Raman spectra contain peaks **related to** specific chemical **bonds**.

Results

Comparison of **the** Brillouin and Raman cartographies reveals correlations between mechanical and chemical properties. **Indeed, the shapes of the phosphate content and stiffness curves are similar.** The two spectroscopies give compatible values for the mean distance between two tubules, i.e., 4-6 µm. **Moreover, for the first time, the daily cross striations of enamel could be studied, indicating a relationship between the variation in the phosphate concentration and the variation in the rigidity within the enamel prisms.**

Conclusions

We demonstrate here the possibility of using Brillouin scattering microscopy to both study complex biological materials such as the enamel-dentin junction and visualize secondary structures. Correlations between the chemical composition and mechanical properties could help in better understanding the tissue histology.

Keywords: enamel, dentin, dentin-enamel junction, Raman microscopy, Brillouin microscopy

1. Introduction

Human teeth are composed of three mineralized materials: cementum, dentin and enamel. Cementum, linked with the periodontal ligament, surrounds the root to fix it in the bony socket. Dentin is the main component of the root and crown, while enamel, in contact with the oral cavity, represents the acellular external part of the crown.

Dental enamel is the hardest tissue of the body, with a high content of **the** mineral phase (96 wt.%), some water (3%) **and** a low content of **a** protein and organic matrix (1%) (Williams et al., 1989). **Enamel is mainly organized into 3-6 µm prisms (also called rods) from the DEJ to the surface**. Dentin contains more minerals (70 wt.%), organic matrix (20 wt.%) and water (10 wt.%) (Nanci, 2017) than enamel. As a consequence, enamel is hard but fragile, while dentin is more elastic. Both have a mineral phase mainly composed of carbonated hydroxyapatite (HAP) (Sydney-Zax et al., 1991). The transition zone between dentin and enamel, called the dentin-enamel junction (DEJ), together with enamel tufts, composed of hypomineralized crack-like defects, plays an important role in the resilience of teeth and **in avoiding crack** propagation (Chai et al., 2009).

The literature describes this interface as a narrow zone corresponding to a transitional domain between the two tissues. Nevertheless, the precise width of this interface is uncertain, and different values have been obtained, depending on the technique used for investigation (Marshall et al., 2003), on the **tooth** origin (Feeney et al., 2010) and on the measurement location (Xu et al., 2009b). **A microhardness** evaluation study estimated the DEJ as a broad, 100 µm wide transition zone (White et al., 2000), whereas another nanoindenter-based study found a width of 10 µm (Chan et al., 2011). **Through** scratching mode AFM, the « functional width » of the **DEJ was introduced, which was** approximatively 2.0 ± 1.1 µm (Habelitz et al., 2001). Scanning and transmission electron microscopy measurements found **widths of** 1 µm and **approximately** 5 µm, respectively (Lin et al., 1993). Histology investigations on embryonic mouse tooth models permitted the DEJ to be described as more than a thin line separating two materials, providing a **spatiotemporal** survey revealing deposition of electron-dense granules, i**.e., intra- and extracellular vesicles highly mineralized observed with transmission electron microscopy**, and a patch of material near the DEJ (Meyer et al., 1999). **This underlines the interest in completing the information on the mechanical properties of the DEJ for the development of new biomaterials.**

The nanomechanical behaviour of the DEJ was intensively investigated by force measurement techniques such as nanoindentation and atomic force microscopy (AFM).

Both techniques require contact between the probe and sample to induce deformation of the material. They provide the so-called reduced Young's modulus E_r, which is related to the Young's modulus and Poisson's ratio ν through $E_r = E/(1-\nu^2)$ for an isotropic material. These techniques allow measurement of peritubular and intertubular dentin, enamel and the DEJ. The experimental results are compiled in *Supplementary Table 1*.

An alternative to these methods is offered by contactless inelastic light scattering-based **microspectroscopies**, which can provide mechanical and chemical maps of the material. In this work, we use Brillouin scattering microscopy to measure the mechanical properties of dentin, enamel and **the** DEJ at the microscopic scale, while Raman scattering is used to explore possible correlations between the mechanical and chemical properties of teeth at the microscopic scale. Indeed, we have **previously** shown that Raman scattering can be used to **obtain** comparative chemical compositions for healthy and carious enamel (Desoutter et al., 2019; Salehi et al., 2013; Slimani et al., 2017). **A previous study based on Brillouin scattering conducted on sagittal and transverse planes of dentin permitted observation of the anisotropy of the collagen fibre network, even with a 1 µm resolution** (Lainović et al., 2020)**.**

Raman scattering allows **assessment of** the different vibrations of hydroxyapatite (HAP) groups (OH 3572 cm^{-1}, ν_1 PO_4^{3-} 960 cm^{-1}, ν_2 PO_4^{3-} 432 cm^{-1} and carbonate CO_3^{2-} 1074 cm^{-1}). The enamel crystal orientation can also be estimated from the intensity of OH bonds, as the maximum is reached when **the** light polarization and bonds are parallel (Tsuda & Arends, 1994). The crystallinity map of the sample can be reconstructed from the intensity ratio of the phosphate Raman peaks at 960 and 950 cm^{-1} or from the inverse of the full-width at half-maximum (FWHM) of the 960 cm^{-1} phosphate peak (Slimani et al., 2017). The correlation between the phosphate Raman peak intensity and mineral density was also investigated in a previous study using microcomputed tomography (Akkus et al., 2016)**.**

Brillouin light scattering (BLS) is based on light wave and acoustic **wave interactions**. It is an emerging technique in biology compared to Raman microscopy (Prevedel et al., 2019). In Brillouin **microspectroscopy**, the frequency shift of the scattered light is related to the longitudinal modulus *M*. The latter is also **related** to the Young's modulus *E* and the Poisson**'s** ratio ν through $M = E(1-\nu)/[(1+\nu)(1-2\nu)]$ for an isotropic material. As shown in the left part of **Fig. 1**, the Young's modulus *E* is the elastic constant for a bar submitted to a stress σ and developing an axial strain ε_L, *i.e.,* $\sigma = E\varepsilon_L$, while the bar is free to contract or expand laterally. *M* is the elastic constant measured when the bar is not free to contract or expand, *i.e.,*

$\sigma = M\varepsilon_L$ with $\varepsilon_\ell = 0$, due to a surrounding material, for example. The Poisson's ratio is the ratio of the lateral contraction/expansion ε_ℓ to the longitudinal **contraction/expansion** ε_L. The right part of **Fig. 1** shows how E_r and M, probed, for example, using nanoindentation or BLS, respectively, differ from E as ν increases towards its maximum value. For $\nu = 0.3$, a typical isotropic average value for enamel and dentin, one expects to measure elastic moduli E_r and M that are ~10% and ~35% higher than E, respectively. BLS probes very high frequency elastic properties (unrelaxed **properties**, higher values) as opposed to, for example, indentation that probes low frequency or quasistatic properties (relaxed **properties**, lower values). While the difference can be small for solid materials such as enamel, elastic values **for softer materials** measured using static or high-frequency techniques can **significantly** differ.

Materials and methods

1.1. Sample preparation

One human mandibular premolar sound **extracted** tooth was washed and stored in 0.2% chlorhexidine disinfectant and kept at 4°C **in distilled water**. **Extraction was performed for orthodontic reasons on a 42-year-old woman.** The approval of the local ethical research committee (process No. 2014-2198) was obtained. **The tooth** was then **longitudinally** sectioned (in the sagittal plane) into slices using a high-speed diamond saw (Isomet 2000, Buehler, USA). Each cross section was 0.5 mm **wide**. Sections were first sanded with a 1200 grit abrasive disc and then polished with diamond pastes of 0.25 and 0.1 µm particle sizes using a polishing machine (Escil, France) to obtain smooth surfaces. Thereafter, the samples were cleaned in an ultrasonic bath, followed by thorough rinsing. Samples were stored in distilled water supplemented with a few drops of chlorhexidine. Finally, samples were dried for half an hour before scans **24 hours after cutting and polishing**.

1.2. Brillouin light scattering

Brillouin spectroscopy uses the **Doppler** frequency shift of the light scattered by the acoustic waves propagating in the sample. Three parameters can be extracted from a Brillouin peak observed in a measured spectrum: the Brillouin frequency shift ν_B, the linewidth of the Brillouin peak Γ_B, and the peak intensity I_B.

In the backscattering geometry, the measured Brillouin frequency shift ν_B is generally related to the longitudinal sound velocity V_L and to the real part of the longitudinal elastic **modulus** M' at GHz frequencies through:

$$M' = \rho V_L^2 = \rho \left(\frac{\lambda_0}{2n}\right)^2 \nu_B^2 \qquad (1)$$

where n is the real part of the refractive index of the medium and ρ is its density. Both n and ρ, or at least ρ/n^2, must be known to obtain M'.

The Brillouin linewidth Γ_B, actually the FWHM of the peak, is related to the dynamic longitudinal viscosity η_L and to the imaginary part of the longitudinal modulus M'':

$$M'' = 2\pi\nu_B\eta_L = \rho \left(\frac{\lambda_0}{2n}\right)^2 \nu_B\Gamma_B \qquad (2)$$

Finally, the relative intensity of the Brillouin peak I_B depends on the ratio of the appropriate squared elasto-optic coefficient p to the elastic constant for a perfectly transparent material:

$$I_B \propto \frac{p^2}{M'} \qquad (3)$$

The above relations are valid for homogenous samples, ***i.e.,* those** with heterogeneities much smaller than $\lambda_0/2n$ within the probed volume. If heterogeneities exist in the scattering volume, **then** multiple Brillouin peaks can be observed according to the different elastic properties. However, if their Brillouin linewidths are too large, **then the peaks** can be difficult to properly separate. Another limit of Brillouin **microspectroscopy** is the use of high NA objectives to achieve high spatial resolution. This comes at the expense of accurate determination of both ν_B and Γ_B, as the former **significantly** depends on the scattered angle.

As mentioned above, both the refractive index and the density are required to compute the elastic moduli. We used the following values from the literature: for dentin, ρ = 1.97 g.cm^{-3} (Schwass et al., 2009) **and** n = 1.54 (Ohmi et al., 2000), and for enamel, ρ = 2.72 g.cm^{-3} (Schwass et al., 2009) **and** n = 1.63 (Hariri et al., 2012).

1.3. Mechanical properties from the Brillouin frequency shift

In Brillouin **microspectroscopy**, the frequency shift of the scattered light is related to the longitudinal modulus M. The latter is also **related** to the Young's modulus E and the **Poisson's**

ratio ν through $M = E(1-\nu)/[(1+\nu)(1-2\nu)]$ for an isotropic material. As shown in the left part of **Fig. 1**, the Young's modulus *E* is the elastic constant for a bar submitted to a stress σ and developing an axial strain ε_L, *i.e.,* $\sigma = E\varepsilon_L$, while the bar is free to contract or expand laterally. *M* is the elastic constant measured when the bar is not free to contract or expand, *i.e.,* $\sigma = M\varepsilon_L$ with $\varepsilon_\ell = 0$, due to **a** surrounding material, for example. The Poisson's ratio is the ratio of the lateral **contraction/expansion** ε_ℓ to the longitudinal contraction/expansion ε_L. The right part of **Fig. 1** shows how E_r and *M*, probed using nanoindentation or BLS, respectively, differ from *E* as ν increases. For $\nu = 0.3$, a typical isotropic average value for enamel and dentin, one expects to measure elastic moduli E_r and *M* that are ~10% and ~35% higher than *E,* respectively. **Furthermore**, it is worth noting that BLS probes very high frequency elastic properties (unrelaxed **properties**, higher values) as opposed to, for example, indentation that probes low frequency or quasistatic properties (relaxed **properties**, lower values). While the difference can be small for solid materials such as enamel, elastic values **for softer materials** measured using static or high-frequency techniques can **significantly** differ. Brillouin spectroscopy has been applied to **obtain** the mechanical properties of biological tissues and materials. However, to the **best** of our knowledge, Brillouin scattering microscopy has not yet been applied to enamel and the dentin-enamel junction.

Fig. 1: Elastic moduli. *Left: difference between the Young's modulus E and the longitudinal elastic modulus M. Right: evolution of the ratio Er/E of the reduced Young's modulus E_r to the Young's modulus E compared to the ratio M/E, where M is the longitudinal Young's modulus as a function of Poisson's ratio ν.*

1.4. Confocal Brillouin microscope

The spectrometer consists of a **multipass** Fabry-**Perot** interferometer of the Sandercock type (Lindsay et al., 1981) coupled to a specially adapted confocal upright microscope (Olympus BX51). As an illumination source, we used a single-mode frequency-doubled DPSS laser with a central wavelength of λ_0 = 532 nm (Excelsior, Spectra-Physics). The illumination output power was **approximately** 50 mW. The reproducibility of the **spectra** measured using this incident power was checked. A high NA = 0.7 100x Mitutoyo objective was used to both illuminate the sample and collect the backscattered light. This setup led to a laser spot diameter

of approximately 0.8 μm. The sample was **mapped** using micropositioning stages (Nano-H100, Mad City Lab) in discrete steps separated by 2 micrometres or 0.5 μm if a better resolution was needed. A typical mapped area of approximately 100×85 μm^2 consisted of 2100 spectra. The acquisition time for one spectrum was approximately 2 min.

1.5. Brillouin data analysis

Brillouin spectra were first corrected for the slight nonlinearity of the Fabry–Perot interferometer scan. Stokes and anti-Stokes Brillouin spectra were then averaged. For each spectrum, Brillouin peaks were **fitted** to damped harmonic oscillator (DHO) response functions $f_{DHO}(\nu)$ with the interferometer resolution $f_r(\nu)$ and the broadening effect of the finite collection aperture $f_c(\nu)$. The DHO response function reads:

$$f_{DHO}(\nu) = I_M \frac{\nu_B^2 \Gamma_B^2}{(\nu^2 - \nu_B^2)^2 + (\nu\Gamma_B)^2}$$

where I_M is the Brillouin peak intensity, ν_B is the frequency shift and Γ_B is the Brillouin linewidth. Alternatively, the Brillouin intensity can be represented through its integrated intensity $I_B = \pi\Gamma_B I_M$. **The interferometer resolution $f_r(\nu)$ is actually given by the shape of the measured central peak, while $f_c(\nu)$ is derived from the known angle dependence of the Brillouin frequency shift and the objective NA used.**

Brillouin frequency shifts of dentin and enamel are expected to appear at quite different frequencies, approximately 24 GHz and 34 GHz, respectively. **Thus**, a first-round analysis consisting of **separately** fitting the two frequency windows was conducted to detect Brillouin peaks corresponding approximately to dentin below 29 GHz and to enamel at higher frequencies. **Approximately** 93% of the Brillouin spectra were actually **composed** of only one peak of statistical significance. **These** spectra were then **fitted** to a single DHO function to obtain the final values of I_M, ν_B and Γ_B of the pixel map.

The first-round analysis also revealed that **approximately** fifty spectra **exhibited** two separated Brillouin peaks with significant intensities. In a second-round analysis, these spectra were adjusted in the 10-40 GHz frequency domain using the sum of two DHO lineshapes. In all cases, one of the Brillouin peaks was found at approximately 24 GHz, while the second peak appeared at approximately 34 GHz, allowing the former to be attributed to dentin and the latter

to enamel. These double-peak spectra were all **obtained from** the DEJ zone, as expected. The remaining ninety spectra did not show any clear Brillouin peak above the background. Except for that from a small hole in the dentin region far from the DEJ, all these spectra were also **obtained from** the DEJ zone and presumably correspond to disordered regions. Such structural disorder at the micron scale generates intense scattering of the incident light, which prevents proper measurement of the Brillouin spectrum.

The boundaries of the DEJ region were obtained using the following method: for each column of the Brillouin map, the DEJ limits were given by a significant drop in the Brillouin intensity, an increase in the Brillouin linewidth or a change in the Brillouin frequency compared to the typical values of the material on the corresponding side. Subsequently, the data analysis of the Brillouin spectra **led** to Brillouin images separated into two distinct regions, dentin and enamel, separated by the DEJ zone.

1.6. Raman microscope

An Alpha300R confocal Raman **microscope** (Witec, Ulm, Germany) with a laser wavelength of 532 nm produced by a frequency-doubled Nd:YAG laser (Newport) **was used**. Linearly polarized light **was** transported to the microscope via a single-mode optical fibre. The system was equipped with a microscope objective from Nikon (Otawara, Japan) with a 20x magnification and a numerical aperture NA = 0.46. The output power at the exit equalled 50 mW, and the theoretical image resolution in the lateral direction was 500 nm. **The integration** time was 0.01 s for each spectrum during an image scan. The size of the scan area was **approximately** 75x75 micrometres, made by 150/200 points per line and 150/200 lines. Data acquisition was performed using Image-Plus 2.08 software from Witec. An edge filter **separated** inelastic backscattered Raman radiation from the Rayleigh signal. The signal **was** collected with an electron-multiplying CCD camera (DU 970N-BV353, Andor, USA) equipped with a 1600×200 pixel chip. The camera controller was a 2.5 MHz 16-bit A/D converter. The system **was** cooled and stabilized at -60°C with a Peltier system. A UHTS 300 spectroscope with a 70% throughput transmission and a grating of 600 lines per mm provided a spectral resolution of 3–5 cm^{-1}. The Raman shift range **was** 200–4000 cm^{-1} (~6 to 120 THz).

Considering the orders of magnitude for the frequency shifts, that is, in the GHz range for Brillouin spectroscopy but in the THz range for Raman spectroscopy, Brillouin spectroscopy is clearly much more demanding in terms of suppression of Rayleigh scattering than Raman spectroscopy. As a consequence, Brillouin **microspectroscopy** and Raman **microspectroscopy**

cannot be performed on the same equipment. To allow relevant comparisons between chemical maps and mechanical property maps, we ensured that Raman and Brillouin scans were **performed** in similar zones. **These** zones were located approximately 60 µm below the cusp tip.

1.7. Raman data analysis

Data analysis provided integrated areas of particular Raman peaks. Data processing was performed using Image Plus software 5.2 from Witec. Each point of the Raman map is related to the area of the peak of interest, which is related to a chemical bond. The area of the integrated peak was converted into a hue for each pixel. The look-up table relates each hue to the peak integration value. In the present mapping, dark hues represent low values and bright yellow hues represent high values of phosphate or organic components.

3. Results

3.1. Experimental spectra

A representative Raman spectrum **of** dentin is plotted in **Fig. 2**D. Raman scattering in dentin and enamel zones produces characteristic peaks related to various chemical bonds that are well established (Salehi et al., 2013). The most intense peak, related to the concentration of HAP, is the phosphate peak at 960 cm^{-1}. The broad peak at 2800-3100 cm^{-1} reveals the presence of proteins, fatty acids and lipids (CH and CH_2): unsaturated bonds of lipids for the 2874 cm^{-1} peak and saturated bonds of lipids for the 2926 cm^{-1} peak (Coello et al., 2015).

Fig. 2: Raman and Brillouin spectra. *Typical Brillouin spectra obtained* ***for*** *A) dentin and B) enamel. C) Brillouin spectrum obtained in the DEJ zone showing two Brillouin peaks. The blue dots are the experimental data, while the red curves are the best adjustments of the data to the harmonic oscillator response functions. D) Raman spectrum of dentin. Note: 1* $cm^{-1} \approx$ *30 GHz.*

Typical Brillouin spectra of dentin and enamel are shown in **Fig. *2***A and 2B. They mainly show the longitudinal acoustic mode at $\nu_B \approx 24$ GHz in dentin and $\nu_B \approx 34$ GHz in enamel. Interestingly, **Fig. *2***C shows a Brillouin spectrum obtained in the DEJ zone, revealing two peaks corresponding to dentin and enamel. However, **spectra with** a single peak or even no peak at all due to disorder **are also observed in this region**, as discussed later.

The Brillouin frequencies observed in dentin and enamel are significantly different **such** that small variations in the elastic properties are better revealed using separate maps. The first **map** focuses on the 20-30 GHz frequency domain and is related to dentin, while the second **map** concentrates on the 30-40 GHz range and enamel.

3.2. Brillouin scattering in dentin

From the spatial dependence of the three parameters extracted from the **analysis of the** Brillouin spectra below **approximately** 30 GHz, we generated the three maps shown in **Fig. 3**A-C, where I_M is plotted in **Fig. 3**A, ν_B in **Fig. 3**B and Γ_B in **Fig. 3**C. We first describe the results obtained in the dentin region outside the DEJ zone. The latter will be discussed at the end of Section 3.

The Brillouin intensity map (**Fig. 3**A) reveals the peculiar structure of dentin in the sagittal plane, made of nearly parallel dentinal microtubules embedded in a mineralized collagen matrix of intertubular dentin. Several lines of low and high intensities are clearly observed, particularly in the bottom left quadrant of the map. These lines are approximately perpendicular to the DEJ and tend to vanish **when** approaching it.

Fig. 3: (Top) Brillouin maps of dentin *close to a junction: A) Brillouin peak intensity I_M, B) Brillouin frequency shift ν_B* ***and*** *C) Brillouin linewidth Γ_B. The white lines are the DEJ boundaries determined as described in the data analysis section.* ***(Middle)*** *Distribution of D) I_M, E) ν_B and F) Γ_B for dentin outside the junction. The red curves are the best Gaussian distributions, giving $\nu_B = 24.6 \pm 0.5$ GHz and $\Gamma_B = 4.7 \pm 0.5$ GHz.* ***(Bottom)*** *Distribution of G) ν_B and H) Γ_B values measured in the bottom left quadrant of maps B-C (red dashed lines).*

*Intertubular regions correspond to I_M values below half of the maximum I_M value detected in the quadrant, while the **tubular** part is the remaining pixels.*

The peritubular dentin, encircling each tubule, is a **hypermineralized** dentinal tissue that should induce a correlated slight increase in the measured Brillouin frequency shift ν_B along these lines (Zhang et al., 2014). As shown in **Fig. 3**A-B, no clear correlation between ν_B and I_M emerges from the maps obtained in this region close to the DEJ, even if some structures appear in the ν_B map. In the dentin region *outside* the DEJ, the measured Brillouin shift values **vary between** approximately 23 and 26 GHz. The average value and standard deviation are 24.6 ± 0.5 GHz (see **Fig. 3**E), a **deviation that is approximately tenfold** larger than that calculated using the same Poisson's ratio value. We obtain $E_r = 28.4 \pm 1.4$ GPa. The mean Young's modulus values obtained in our study are in agreement with literature data reported in (Zhang et al., 2014), provided that they were obtained in similar dry conditions according to the timescale of the Brillouin mapping experiment. As **previously** mentioned, the elastic properties are indeed sensitive to a series of external conditions. Moreover, our range of values in dentin are very close to those recently obtained using Brillouin light scattering, where the longitudinal modulus **was** evaluated to **be** 36 GPa along a similar sagittal plane but not close to the DEJ (Lainović et al., 2020).

Following the method used in (Lainović et al., 2020), we attempted to numerically explore the correlation between ν_B and I_M by defining a Brillouin peak intensity threshold $I_{M_{th}}$ equal to half the maximum value. To avoid artefacts due to the proximity of the DEJ, we restricted the analysis to the bottom left quadrant of the map indicated by the red dashed lines in **Fig. 3**A-C. The distribution of the ν_B values in the two subgroups is plotted in **Fig. 3**G as boxplots in red together with violin plots in blue for the probability density. According to the output of an unpaired two-tailed *t* test giving a level of significance $p < 10^{-6}$, the frequency shift is slightly larger in the high intensity regions **(peritubular regions)** than in the **low intensity regions**, in agreement with the experimental data shown in (Lainović et al., 2020). This result is difficult to interpret, as the Brillouin intensity should decrease in the peritubular **regions** due to the empty dentinal tubules. Finally, we note that including data closer to or even from the DEJ tends to **destroy** such a correlation between the Brillouin peak intensity and frequency shift, with the level of significance *p* approaching unity. The proximity of the DEJ probably **perturbates** the correct measurement of the Brillouin intensity, for example, due to an increase in surface roughness, disorder…

Using eq. (1) with the density and refractive index values quoted in the Materials and Methods section, our Brillouin shift values lead to the following longitudinal elastic **modulus** and standard deviation: $M' = 35.6 \pm 1.8$ GPa. Assuming an isotropic average Poisson's ratio $\nu = 0.31$ for dentin (Richert et al., 2020), the longitudinal modulus M' estimated in the dentin zone gives a mean Young's modulus $E = 25.7 \pm 1.3$ GPa. For a more direct comparison with values extracted from nanoindentation or AFM studies, the corresponding reduced Young's modulus E_r can be calculated using the same Poisson's ratio value.

Finally, the map of the Brillouin linewidth Γ_B presented in **Fig. 3**C does not show any clear correlation with the two other maps. **When** restricted to the bottom left quadrant, an unpaired two-tailed *t* test leads to a poor level of significance $p < 10^{-3}$(see **Fig. 3**H). The approximate **Gaussian** distribution of the linewidth centred on $\Gamma_B = 4.7 \pm 0.5$ GHz (see **Fig. 3**F) seems to be well scattered **over** the entire map except for the largest values, which appear to be more localized in the softer region close to the DEJ or around the defect at the bottom of the map. The large broadening of the Brillouin peaks in the dentin region could be ascribed **to a change in the viscosity** of the complex material in the scattering volume. Following eq. (2), the estimated mean dynamic viscosity would be **approximately** 0.05 Pa.s.

Fig. 4A **shows** a map of the intensity of the Raman peak at approximately 2800 cm^{-1} in dentin and thus of the protein concentration in the scattering volume. The intensity of the scattered light ranges from $1.3x10^5$ to $3.3x10^5$ counts on the CCD for the dark and yellow hues, respectively. The lowest intensity is far larger than the minimal intensity that **can be measured** with our experimental device. **Thus**, even the dark zones in **Fig. 4**A contain proteins. The intensity profile as a function of the position in the sample for the region highlighted by the blue box in **Fig. 4**A is plotted in **Fig. 4**B. Some microstructures are visible due to variations in the protein concentration on a characteristic length scale on the order of 5 µm. To compare the chemical map with the mechanical properties of dentin, we plot in **Fig. 4**C a zoom in of **Fig. 3**A centred on the dentin area. The Brillouin intensity profile averaged in the red box is shown in **Fig. 4**D as a solid red line. It also exhibits clear variations that can be compared to those observed in the chemical map (**Fig. 4**A-B) when the **eightfold** difference in the image resolution is taken into account. The **downsampled** Raman intensity profile of **Fig. 4**B plotted in **Fig. 4**D as a blue dashed line **indeed** looks very similar to the Brillouin intensity profile. **Fig. 4**B and

Fig. 4D show that variations in the dentin chemical composition lead to variations in its mechanical properties, **as** observed in previous microhardness (Habelitz et al., 2001; Ziskind et al., 2011) and Brillouin (Lainović et al., 2020) studies of inter- and peritubular human dentin.

Fig. 4: Comparison of Raman and Brillouin images across dentin tubules. *A) Chemical map of dentin obtained with the 2800 cm^{-1} (protein) Raman peak intensity; B) protein peak intensity profile along the blue rectangle in image A; C) Brillouin peak intensity I_M* ***map*** *of dentin; D) Brillouin peak intensity profile along the red rectangle in image C (red solid line) compared to the* ***downsampled*** *protein peak intensity profile (blue dashed line).*

3.3. Brillouin scattering in enamel

We now focus on the Brillouin maps of enamel displayed in **Fig. 5** together with the distribution of the three parameters I_M, ν_B and Γ_B. The variability of the latter parameters is less pronounced than in the dentin region, in agreement with the enamel composition being essentially crystalline hydroxyapatite. In homogeneous transparent materials, the elasto-optic coefficients *p* related to the longitudinal acoustic modes are generally larger for soft materials (lower M' values) than for hard **materials** (higher M' values). Following eq. (3), we anticipate higher Brillouin intensities in the dentin region than in the enamel region. As seen in **Fig. 5**A and **Fig. 3**A, this is to a large extent the case, as the average dentin Brillouin peak intensity is **approximately** 1.5-fold larger than the enamel peak intensity (and 3.6-fold larger for the integrated Brillouin intensity). I_M also shows smaller deviations outside the DEJ in enamel that **amount** to approximately ± 20% (see **Fig. 5**D), instead of **approximately** ± 50% in dentin, and without any clear pattern in this region close to a DEJ.

Fig. 5*: (Top) Brillouin maps of enamel close to a junction: A) Brillouin peak intensity I_M, B) Brillouin frequency shift ν_B and C) Brillouin linewidth Γ_B. The white lines are the DEJ boundaries determined as described in the data analysis section.* ***(Bottom) Distribution of*** *D) I_M, E) ν_B and F) Γ_B for enamel outside the junction. The red curves are the best Gaussian distributions, giving $\nu_B = 34.2 \pm 0.2$ GHz and $\Gamma_B = 2.0 \pm 0.3$ GHz.*

Outside the DEJ, the variation in ν_B results in a mean value and **a** standard deviation of 34.2 ± 0.2 GHz (see **Fig. 5**E). We note, however, that most of the lowest values are found close to the DEJ. Following eq. (1), the longitudinal elastic modulus M' is estimated to be 84.7 ± 1.0 GPa in this scanned region, whereas $E = 66.3 \pm 0.8$ GPa and $E_r = 71.9 \pm 0.9$ GPa **when** using $\nu = 0.28$ (Lees & Rollins Jr, 1972).

The map of the Brillouin linewidth Γ_B presented in **Fig. 5**C reveals a quite homogeneous material with an average value of 2.0 ± 0.2 GHz (see Fig. 5F) for enamel. Despite the high **content** of the mineral phase, Γ_B does not exhibit the typical low values observed in pure crystalline solids, which are usually related to the "network viscosity". This is partly due to the anisotropy of the elastic moduli probed by the high numerical aperture as well as to the random HAP crystallite orientation in the basal plane. The small amount of water and organic compounds should also participate in sound wave attenuation.

We further probed the outer enamel region of a different slice of **the** tooth using Brillouin and Raman scattering. **Fig. 6**A shows a typical optical image of outer enamel in the sagittal plane at the sample surface obtained as described in Section 2.1. The Brillouin frequencies measured in the white rectangular frame with a spatial resolution of 0.5 µm are plotted in **Fig. 6**B. They clearly evolve between 34.6 and 36.4 GHz in the scanned area, denoting significant changes in the related elastic moduli of **approximately** 10% **according to eq. (1) and the indices and densities of enamel and dentin given in Section 1.2**. These variations reveal almost parallel lines of high Brillouin frequency values in agreement with the direction of the HAP prisms. Furthermore, an approximately 4 µm-length modulation of the Brillouin frequency shift values is also observed in the central high frequency value region, presumably attributed to the enamel cross striations. As a comparison, **Fig. 6**C shows a map of the PO_4^{3-} Raman peak intensity of enamel in a similar region (enamel rod) of a different tooth **slice**. In the latter image, **a** dark hue represents **a** low peak intensity, whereas a bright hue stands for **a** high peak intensity **and** thus more mineralized enamel material. We expect more mineralized enamel material to be stiffer, thus exhibiting higher Brillouin frequency values. Both the directions of the prism and the cross striations are clearly visible. We note, however, that the Raman and Brillouin maps do not entirely coincide, as the high Brillouin frequency values form ~1 µm-thick lines, whereas the high Raman intensity values clearly form ~4 µm-thick regions. **Using eq. (1) and the values**

found, we can affirm that the difference between the modulus at the centre of the regular striations and that of the surrounding material is approximately 0.3 GPa.

Fig. 6: *A) Optical image of the enamel region probed using Brillouin scattering. B) Corresponding Brillouin frequency shift ν_B image. C) Typical PO_4^{3-} Raman peak intensity image in the enamel region of a* ***tooth*** *at the same scale.*

3.4. Brillouin scattering in the dentin-enamel junction region

We finally concentrate on the intermediate DEJ zone. Looking at the Brillouin maps shown in **Fig. 3** and **Fig. 5**, we observe that this region is very complex to describe. **Among** the 385 Brillouin spectra **that** have been ascribed to the DEJ following the method detailed in Section 2.4, 53 **contain** a Brillouin peak related to **the** dentin material, 184 **contain a peak related** to **the** enamel material, **and** 25 spectra show both Brillouin peaks. Presumably due to the strong disorder, the remaining 123 spectra display no clear peak at all, leading to an incomplete map of the elastic properties in this region. Comparing the surface of the DEJ **along** its length in the investigated zone, the mean width of the transitional zone detected with BLS is roughly estimated to be approximately 16 ± 2 µm. However, as observed in **Fig. 3** and **Fig. 5**, the width **significantly** varies along the DEJ in this region.

As expected, the Brillouin peak intensity values I_M detected in the DEJ zone are clearly lower than those corresponding to the same material far from the DEJ, whereas the Brillouin linewidth Γ_B is often significantly larger. Conversely, the Brillouin shift values are in most cases in the range of those found for dentin or enamel **outside** of the DEJ. Interestingly, the dentin material is found in only one subregion of the DEJ, almost crossing the transitional zone, as seen in **Fig. 3**B. A Brillouin peak corresponding to **the** enamel material is more frequently observed in the DEJ and **quasisystematically** on the enamel side (see **Fig. 5**B). However, a large zone close to the dentin side contains solely a Brillouin peak related to **the** enamel material. In such areas,

one would be tempted to describe the DEJ as a quite sharp transition from **the** dentin to enamel material, whereas at other places, the transitional DEJ region seems much more gradual.

We now compare the transitional zone between enamel and dentin using the chemical and mechanical maps **obtained** from Raman and Brillouin scattering, respectively. As an illustration, a map of the Raman peak related to **the** phosphate concentration is plotted in **Fig. 7**A, and a map of the Brillouin shift is shown in **Fig. 7**C. The three zones previously identified, dentin (D), enamel (E) and the DEJ interface, are also observed in **Fig. 7**A. **Fig. 7**B shows the intensity profile of the phosphate peak averaged over the blue box in **Fig. 7**A as a blue solid line, while the red dashed line is the intensity profile of the Raman protein peak in the same region. From such profiles, a transitional width can be extracted. The mean value over the complete map is found to be 13.4 ± 3.1 μm, in fair agreement with the values extracted from Brillouin **microscopy** as well as from a previous Raman microscopy study (Xu et al., 2009a). **Fig. 7**D shows the profiles of the Brillouin shift (red line), Brillouin intensity (green line) and Brillouin linewidth (blue line) along the red line drawn in **Fig. 7**C. All the parameters displayed in **Fig. 7**B and **Fig. 7**D show a rapid variation across the DEJ transition zone, from the values observed in the dentin region to the values found in the enamel region. Note that the rather strong and rapid variations in the Brillouin intensity in the dentin zone are related to the discussion of Fig. 4D.

We observe that the profiles extracted from the **intensities** of the phosphate peak and the protein peak (see **Fig. 7**B) clearly show continuous variations. This obviously **occurs** because the two molecular species exist in both dentin and enamel. Only their respective **concentrations** are changing. Those changes are, however, faster in a restricted zone ascribed to the DEJ, whose width is **approximately** 15 μm. **In contrast**, the profiles derived from the Brillouin maps (see **Fig. 7**D) reveal rather sharp discontinuities of the parameters across the DEJ zone. In **Fig. 7**D, one also observes the presence of two Brillouin peaks in the same scattering volume, one from enamel and one from dentin. This information cannot be obtained from the Raman profiles shown in **Fig. 7**B.

Fig. 7: DEJ in Raman and Brillouin maps. A) Map of the phosphate intensity peak from Raman microspectroscopy; B) profile of the intensity of the phosphate peak averaged over the **blue** box in A; C) map of the Brillouin frequency shift; D) profiles of the Brillouin shift (red

line) $\boldsymbol{\nu_B}$, intensity (green line) $\boldsymbol{I_B}$ and linewidth (blue line) $\boldsymbol{\Gamma_B}$. Brillouin shifts and linewidths are **related** to the left scale, whereas Brillouin intensities are related to the **right** scale. Dots refer to dentin, whereas squares refer to enamel. **The zero position is related to the left part of the red line shown in C in the dentin.**

Discussion

Brillouin microscopy, using a Sandercock-type interferometer, allows not only complete study of enamel, dentin and its junction but also visualization of, through Brillouin frequency shift mapping, secondary structures such as the cross striations inside the enamel prism. To our knowledge, this is the first Brillouin shift mapping of enamel and dental cross striations. This study of the mechanical and viscoelastic properties completes the dental histology described by optical microscopy.

A significant difference in the frequency shift between a stiffer part, attributed to the area around a tubule, and the softer material between two tubules could be highlighted ($p<10^{-6}$). This is consistent with the PTD and ITD composition and with the chosen resolution of 2 µm, close to the mean diameter of tubules (Schilke et al., 2000)**.**

Concerning enamel, the values found in different scans are consistent with previous studies on mechanical properties. Indeed, even if direct comparison of the elastic modulus value is not possible due to the difference in frequency of solicitation, the range of present measurements is quite close to that of previous nanoindentation measurements (Zhang et al., 2014)**. For both enamel and dentin, our results are consistent with the orders of magnitude of Young's moduli found by nanoindentation (see Supplementary Table 1).**

Enamel is organized in rods in a direction more or less similar to the enamel tubules. However, the enamel localized in such an area close to the DEJ is without any pattern, called aprismatic enamel. In enamel rods, internal variations of HAP could be highlighted. These variations are the result of the circadian cycle of ameloblast mineral secretion/maturation (Desoutter et al., 2019). Chemical variations in the PAH concentration and mechanical variations are spatially correlated: where the PAH concentration is higher, the **Brillouin** shift and thus stiffness **are** higher, and vice versa.

The Brillouin shift map, even if noisier than the chemical Raman maps, is correlated with the stiffness variation inside enamel prisms. There has never been a mechanical study of enamel cross striations. This is a sample of a limited area in 2D, whereas the structure of enamel requires a broader comprehension over its entire thickness to fully understand the functioning of the overall resilience.

The values found in the regular variations of the enamel allow us to formulate the hypothesis of a spring/damper type of behaviour (Zahalka & Ellermann, 2017)**.**

At the DEJ, the results indicate that the profiles derived from the two techniques behave differently. The profiles extracted from the **intensities** of the phosphate peak and the protein peak clearly show a progressive increase in phosphate species together with a progressive decrease in **the** protein content from the dentin zone to the enamel zone. These changes are restricted to the DEJ, whose chemical width is estimated to be **approximately** 15-17 μm. **The mechanical** width of the DEJ is similar. **However**, the mechanical variations reveal sharp discontinuities. **We note that this value is also rather close to the width obtained from previous Raman microscopy studies, approximately 12-15 and 13 μm** (Xu et al., 2009a; Slimani et al., 2017)**.** Brillouin microscopy in such zones shows a lower shift compared to the rest of the enamel far from the DEJ, corresponding to the mix between the enamel and dentin frequency shifts and to enamel and dentin peaks in the same spectrum.

The differences between the two Brillouin and Raman **profiles** at the DEJ are consequences of fundamental differences in the spectroscopies. Photon/acoustic phonon interactions in Brillouin scattering need a sufficient diffusion volume to permit phonon propagation. The smallest length to obtain a signal, called the acoustic wavelength scale L_A, is in the range of a few hundred **nanometres**, depending **on the** refractive index n and wavelength of incident light λ, related by $L_A=\lambda/2n$ (Prevedel et al., 2019), **i.e., in our study, approximately 170 nm.** For propagation and interaction with photons, the acoustic wave needs sufficient space. **The component scale L_C, i.e., the length of a homogenous material, needs to have a critical size. The short L_C values of dentin or enamel could alter the Brillouin signal. In contrast**, Raman scattering is based on photon/optical phonons, and even a very small diffusion volume **can** generate a signal. For Brillouin scattering, the DEJ zone is mostly seen as an inhomogeneous or an altered region at the interface between dentin and enamel. The two different materials coexist, giving rise to one or two Brillouin peaks according to the content of each material in the scattering volume provided that their thickness is larger than a couple times the acoustic wavelength. We note, however, that at some other points in the DEJ, intermediate Brillouin scattering frequency values are observed, indicating that in this case, an effective medium is probed. Inspecting all the DEJ zones, we further observe that the Brillouin peak related to dentin rapidly disappears on the dentin side of the DEJ, within approximately 5 μm, while the Brillouin peak associated with enamel is often **well** detected, even if the Brillouin intensity rapidly decreases, as can be seen. **This could suggest that the dentin abruptly stops** where the enamel begins.

Concerning the phosphate peak intensity in Raman scattering, as enamel located at the DEJ contains a lower level of HAP than the outer enamel, the profile is smoother. Conversely, the profile of the protein peak intensity indicates a faster decay than that of phosphate.

The two spectroscopies give apparently concordant results about the abrupt dentin stop and the smooth phosphate transition. The concordance between the abrupt variations in the protein content and viscoelastic properties suggests that the protein strongly influences the tissue mechanical properties. Beyond the fundamental analysis of the DEJ chemical and mechanical properties lie important data to develop new **biomaterials** mimicking the load accommodation of the DEJ. For the bonding of ceramic **crowns**, it is also important to follow the tooth and prosthodontic surface deformation under mechanical stress to avoid tooth enamel degradation by a rigid ceramic (Davidenko et al., 2021).

Finally, the characteristic size of the transitional zone between dentin and enamel cannot be considered as an invariant **or** a geometrically well-defined area where all physical and chemical quantities vary in a similar way, as enlightened by the new Brillouin scattering experiment. **Accumulation of data could give a more reliable picture of the DEJ**. A solution to solve the problem **of long-time scanning** could be the use of a virtually imaged phased array (VIPA) (Shirasaki, 1999)-based spectrometer. Spectrographs built with VIPA **components** have lower contrast than FPT-based **designs**, but they have shorter integration **times** and could allow **the** accumulation of spectra in a reasonable time**. Systems based on one or more VIPAs, coupled with contrast enhancement systems such as iodine tanks, special masks on Fourier planes, multiexcitation systems or Fabry-Perot interferometers - as is currently being studied** (Edrei et al., 2017; Prevedel et al., 2019; Troyanova-Wood & Yakovlev, 2021) **- could allow combining of a high speed of acquisition with sufficient contrast to open an era of study of mineralized tissues, bones and teeth in particular.**

Conclusion

Our work demonstrates the appropriateness of Brillouin **microscopy** as a **nondestructive** method to reveal valuable information on tooth tissue regarding its mechanical properties, such as elastic modulus and viscosity. **This novel technique for biological samples is complementary to Raman microscopy.** Employing such multimodal investigation revealed important differences in the DEJ definition. Moreover, the relation between **information** from Brillouin spectroscopy and Raman spectroscopy could help in better understanding the mechanical **behaviour** of the tooth during chemical modifications. The experimental methods presented in the article can be used for other dental materials, providing important mechanical and chemical information to allow a wiser clinical decision in their use. **The combination** of Brillouin microscopy and **holographic interferometry** would be useful for describing the **behaviour** of new **cements** and new **biomaterials** mimicking the **ability of the DEJ** to prevent enamel cracks and destruction. **New developments in Brillouin microscopy techniques, by coupling a fast acquisition time with a VIPA component and high contrast, will allow the transfer of such techniques to dentistry.**

Akkus, A., Akkus, O., Roperto, R., & Lang, L. (2016). Investigation of Intra-and Inter-individual Variations of Mineralisation in Healthy Permanent Human Enamel by Raman Spectroscopy. *Oral Health and Preventive Dentistry*, *14*(4), 321-327.

Chai, H., Lee, J. J.-W., Constantino, P. J., Lucas, P. W., & Lawn, B. R. (2009). Remarkable resilience of teeth. *Proceedings of the National Academy of Sciences*, *106*(18), 7289-7293.

Chan, Y. L., Ngan, A. H. W., & King, N. M. (2011). Nano-scale structure and mechanical properties of the human dentine–enamel junction. *Journal of the mechanical behavior of biomedical materials*, *4*(5), 785-795.

Coello, B., López-Álvarez, M., Rodríguez-Domínguez, M., Serra, J., & González, P. (2015). Quantitative evaluation of the mineralization level of dental tissues by Raman spectroscopy. *Biomedical Physics & Engineering Express*, *1*(4), 045204.

Davidenko, N. A., Zheng, X., Davidenko, I. I., Pavlov, V. A., Chuprina, N. G., Kuranda, N., Studzinsky, S. L., Pandya, A., Mahdi, H., & Ladak, A. (2021). Holographic Interferometry Real Time Imaging of Refraction Index 2D Distribution and Surface Deformations in Biomedicine. *BIOIMAGING*, 216-220.

Desoutter, A., Slimani, A., Al-Obaidi, R., Barthélemi, S., Cuisinier, F., Tassery, H., & Salehi, H. (2019). Cross striation in human permanent and deciduous enamel measured with confocal Raman microscopy. *Journal of Raman Spectroscopy*, *50*(4), 548-556.

Edrei, E., Gather, M. C., & Scarcelli, G. (2017). Integration of spectral coronagraphy within VIPA-based spectrometers for high extinction Brillouin imaging. *Optics express*, *25*(6), 6895-6903.

Feeney, R. N., Zermeno, J. P., Reid, D. J., Nakashima, S., Sano, H., Bahar, A., Hublin, J.-J., & Smith, T. M. (2010). Enamel thickness in Asian human canines and premolars. *Anthropological Science*, *118*(3), 191-198.

Habelitz, S., Marshall, S. J., Marshall Jr, G. W., & Balooch, M. (2001). The functional width of the dentino-enamel junction determined by AFM-based nanoscratching. *Journal of structural biology*, *135*(3), 294-301.

Hariri, I., Sadr, A., Shimada, Y., Tagami, J., & Sumi, Y. (2012). Effects of structural orientation of enamel and dentine on light attenuation and local refractive index : An optical coherence tomography study. *Journal of Dentistry*, *40*(5), 387-396. https://doi.org/10.1016/j.jdent.2012.01.017

Lainović, T., Margueritat, J., Martinet, Q., Dagany, X., Blažić, L., Pantelić, D., Rabasović, M. D., Krmpot, A. J., & Dehoux, T. (2020). Micromechanical imaging of dentin with Brillouin microscopy. *Acta Biomaterialia*, *105*, 214-222.

Lees, S., & Rollins Jr, F. R. (1972). Anisotropy in hard dental tissues. *Journal of Biomechanics*, *5*(6), 557-566.

Lin, C. P., Douglas, W. H., & Erlandsen, S. L. (1993). Scanning electron microscopy of type I collagen at the dentin-enamel junction of human teeth. *Journal of Histochemistry & Cytochemistry*, *41*(3), 381-388.

Lindsay, S. M., Anderson, M. W., & Sandercock, J. R. (1981). Construction and alignment of a high performance multipass vernier tandem Fabry–Perot interferometer. *Review of scientific instruments*, *52*(10), 1478-1486.

Marshall, S. J., Balooch, M., Habelitz, S., Balooch, G., Gallagher, R., & Marshall, G. W. (2003). The dentin–enamel junction—A natural, multilevel interface. *Journal of the European Ceramic Society*, *23*(15), 2897-2904.

Meyer, J. M., Bodier-Houlle, P., Cuisinier, F. J. G., Lesot, H., & Ruch, J. V. (1999). Initial aspects of mineralization at the dentino-enamel junction in embryonic mouse incisor in vivo and in vitro : A tem comparative study. *In Vitro Cellular & Developmental Biology-Animal*, *35*(3), 159-168.

Nanci, A. (2017). *Ten Cate's Oral Histology-e-book : Development, structure, and function*. Elsevier Health Sciences.

Ohmi, M., Ohnishi, Y., Yoden, K., & Haruna, M. (2000). In vitro simultaneous measurement of refractive index and thickness of biological tissue by the low coherence interferometry. *IEEE Transactions on Biomedical Engineering*, *47*(9), 1266-1270.

Prevedel, R., Diz-Muñoz, A., Ruocco, G., & Antonacci, G. (2019). Brillouin microscopy : An emerging tool for mechanobiology. *Nature methods*, *16*(10), 969-977.

Richert, R., Farges, J.-C., Tamimi, F., Naouar, N., Boisse, P., & Ducret, M. (2020). Validated Finite Element Models of Premolars : A Scoping Review. *Materials*, *13*(15), 3280. https://doi.org/10.3390/ma13153280

Salehi, H., Terrer, E., Panayotov, I., Levallois, B., Jacquot, B., Tassery, H., & Cuisinier, F. (2013). Functional mapping of human sound and carious enamel and dentin with Raman spectroscopy. *Journal of biophotonics*, *6*(10), 765-774.

Schilke, R., Lisson, J. A., Bauß, O., & Geurtsen, W. (2000). Comparison of the number and diameter of dentinal tubules in human and bovine dentine by scanning electron microscopic investigation. *Archives of oral biology*, *45*(5), 355-361.

Schwass, D. R., Swain, M. V., Purton, D. G., & Leichter, J. W. (2009). A system of calibrating microtomography for use in caries research. *Caries Research*, *43*(4), 314-321. https://doi.org/10.1159/000226230

Shirasaki, M. (1999). Virtually imaged phased array. *Fujitsu Scientific & Technical Journal*, *35*(1), 113-125.

Slimani, A., Nouioua, F., Desoutter, A., Levallois, B., Cuisinier, F. J., Tassery, H., Terrer, E., & Salehi, H. (2017). Confocal Raman mapping of collagen cross-link and crystallinity of human dentin–enamel junction. *Journal of biomedical optics*, *22*(8), 086003.

Sydney-Zax, M., Mayer, I., & Deutsch, D. (1991). Carbonate content in developing human and bovine enamel. *Journal of dental research*, *70*(5), 913-916.

Troyanova-Wood, M. A., & Yakovlev, V. V. (2021). Multi-wavelength excitation Brillouin spectroscopy. *IEEE Journal of Selected Topics in Quantum Electronics*, *27*(4), 1-5.

Tsuda, H., & Arends, J. (1994). Orientational micro-Raman spectroscopy on hydroxyapatite single crystals and human enamel crystallites. *Journal of Dental Research*, *73*(11), 1703-1710.

White, S. N., Paine, M. L., Luo, W., Sarikaya, M., Fong, H., Yu, Z., Li, Z. C., & Snead, M. L. (2000). The dentino-enamel junction is a broad transitional zone uniting dissimilar bioceramic composites. *Journal of the American Ceramic Society*, *83*(1), 238-240.

Williams, P. L., Warwick, R., Dyson, M., & Bannister, L. H. (1989). Gray's anatomy 37th ed. *Churchill Livingstone, Edinburgh*.

Xu, C., Yao, X., Walker, M. P., & Wang, Y. (2009a). Chemical/molecular structure of the dentin–enamel junction is dependent on the intratooth location. *Calcified tissue international*, *84*(3), 221.

Xu, C., Yao, X., Walker, M. P., & Wang, Y. (2009b). Chemical/Molecular Structure of the Dentin–Enamel Junction is Dependent on the Intratooth Location. *Calcified Tissue International*, *84*(3), 221. https://doi.org/10.1007/s00223-008-9212-8

Zahalka, C., & Ellermann, K. (2017). Determining a Function for the Damping Coefficient of a laminated Stack. *Technische Mechanik*, *37*(2-5), 161-170.

Zhang, Y.-R., Du, W., Zhou, X.-D., & Yu, H.-Y. (2014). Review of research on the mechanical properties of the human tooth. *International journal of oral science*, *6*(2), 61.

Ziskind, D., Hasday, M., Cohen, S. R., & Wagner, H. D. (2011). Young's modulus of peritubular and intertubular human dentin by nano-indentation tests. *Journal of structural biology*, *174*(1), 23-30.

Young's Modulus
Lateral expansion

Longitudinal Modulus
No lateral expansion

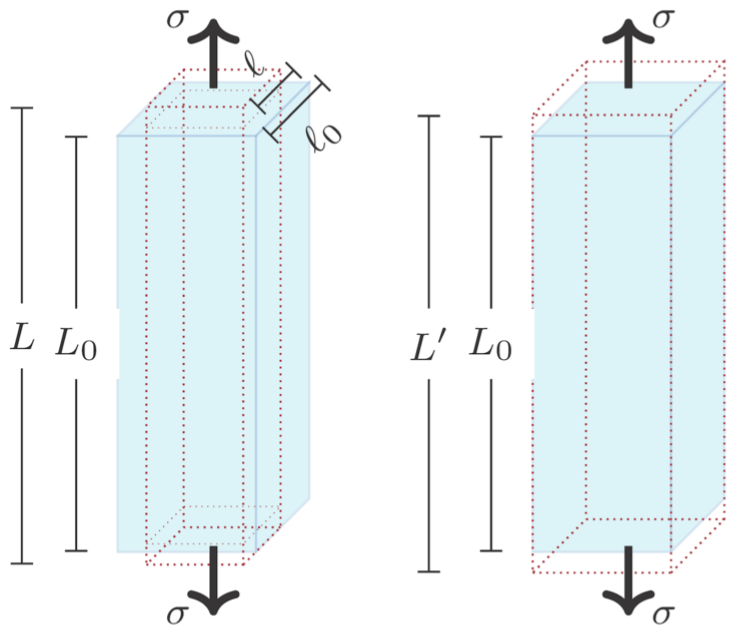

$$E = \frac{\sigma}{\epsilon_{\mathrm{L}}}\ ,\ \nu = \frac{\epsilon_{\mathrm{L}}}{\epsilon_{\ell}} \qquad M = \frac{\sigma}{\epsilon'_{\mathrm{L}}}\ ,\ \epsilon_{\ell} = 0$$

$$\epsilon_{\mathrm{L}} = \frac{L - L_0}{L_0}\ ,\ \epsilon_{\ell} = \frac{\ell - \ell_0}{\ell_0} \qquad \epsilon_{\mathrm{L}'} = \frac{L' - L_0}{L_0}$$

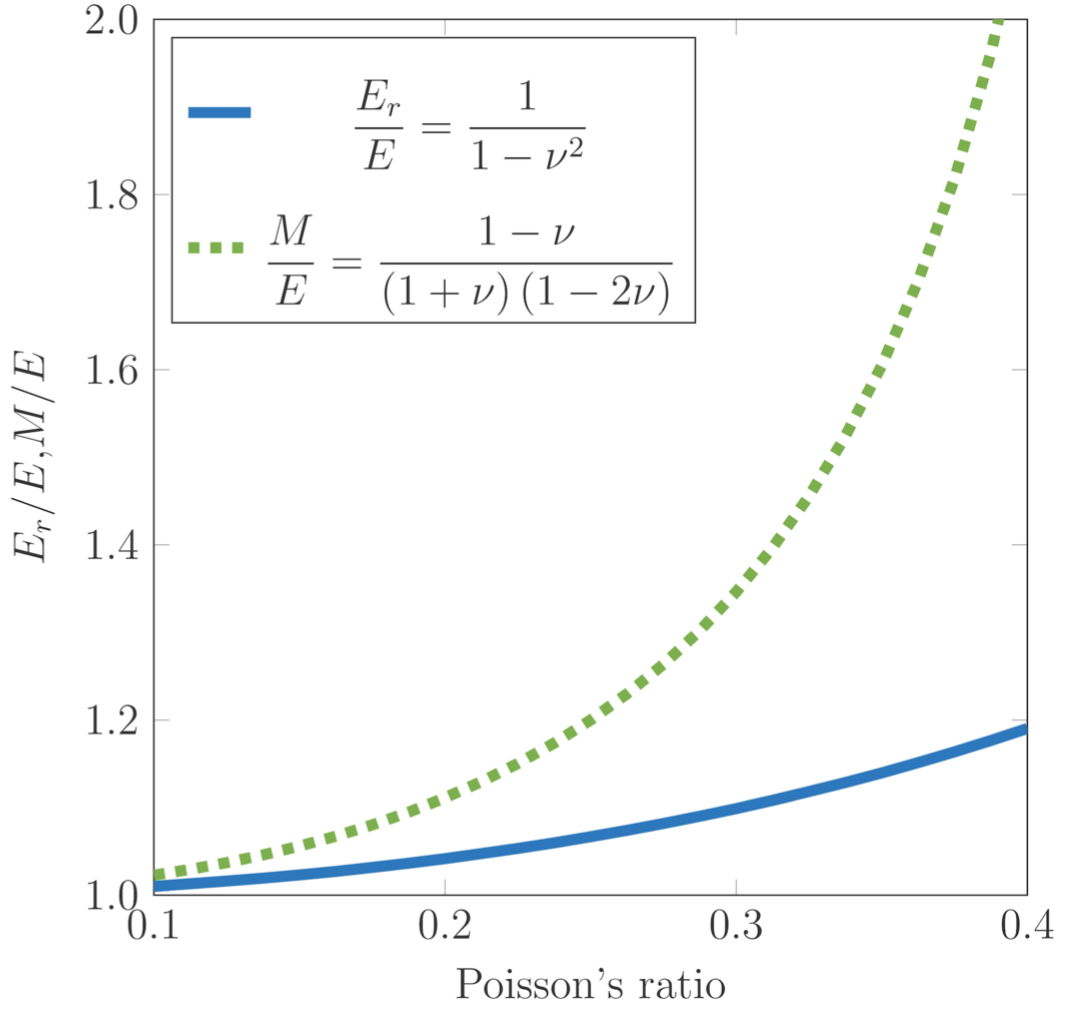

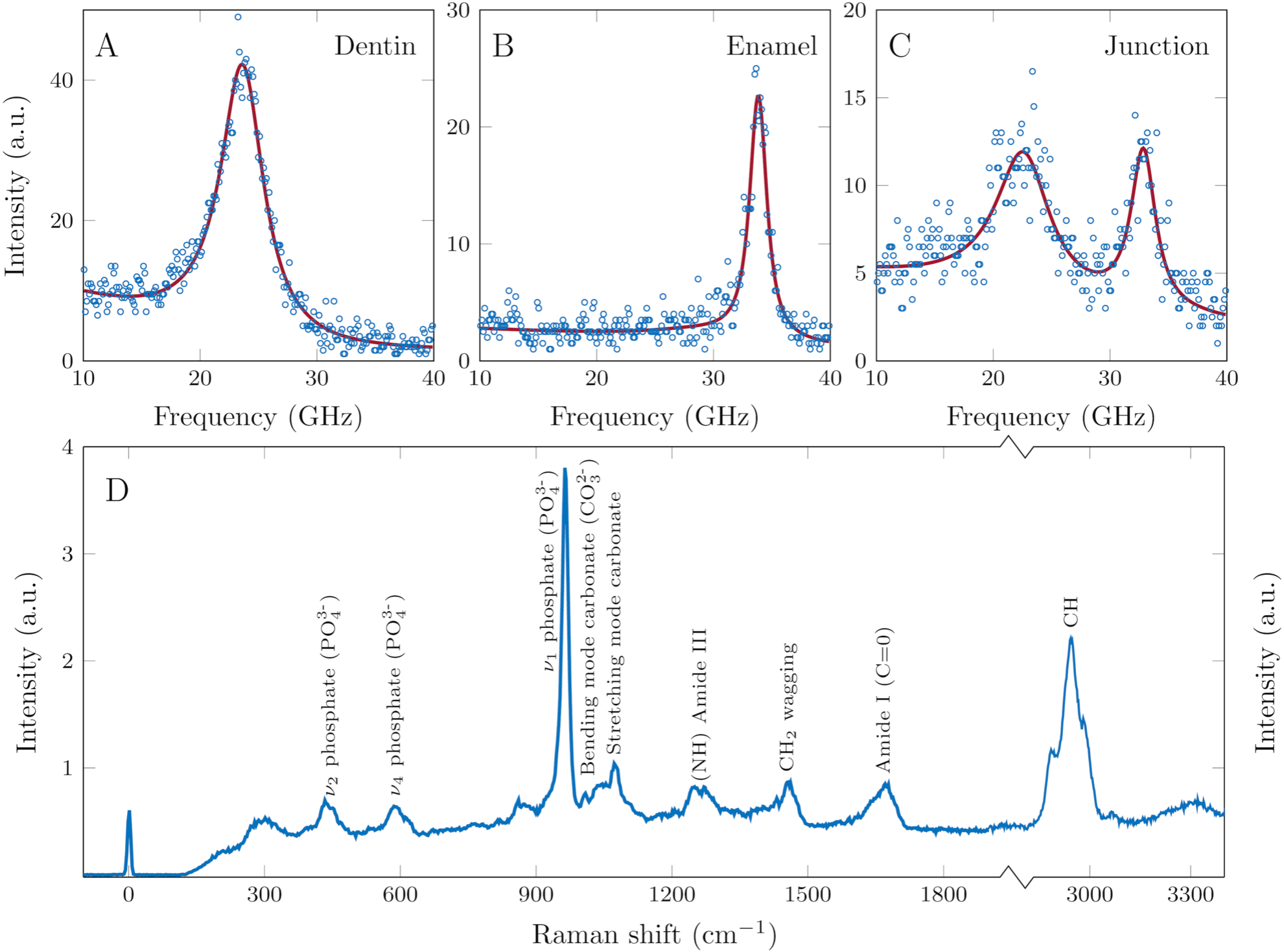
A
Dentin
B
Enamel
C
Junction
Intensity (a.u.)
Frequency (GHz)
Frequency (GHz)
Frequency (GHz)
D
ν_2 phosphate (PO_4^{3-})
ν_4 phosphate (PO_4^{3-})
ν_1 phosphate (PO_4^{3-})
Bending mode carbonate (CO_3^{2-})
Stretching mode carbonate
(NH) Amide III
CH_2 wagging
Amide I (C=0)
CH
Intensity (a.u.)
Intensity (a.u.)
Raman shift (cm^{-1})

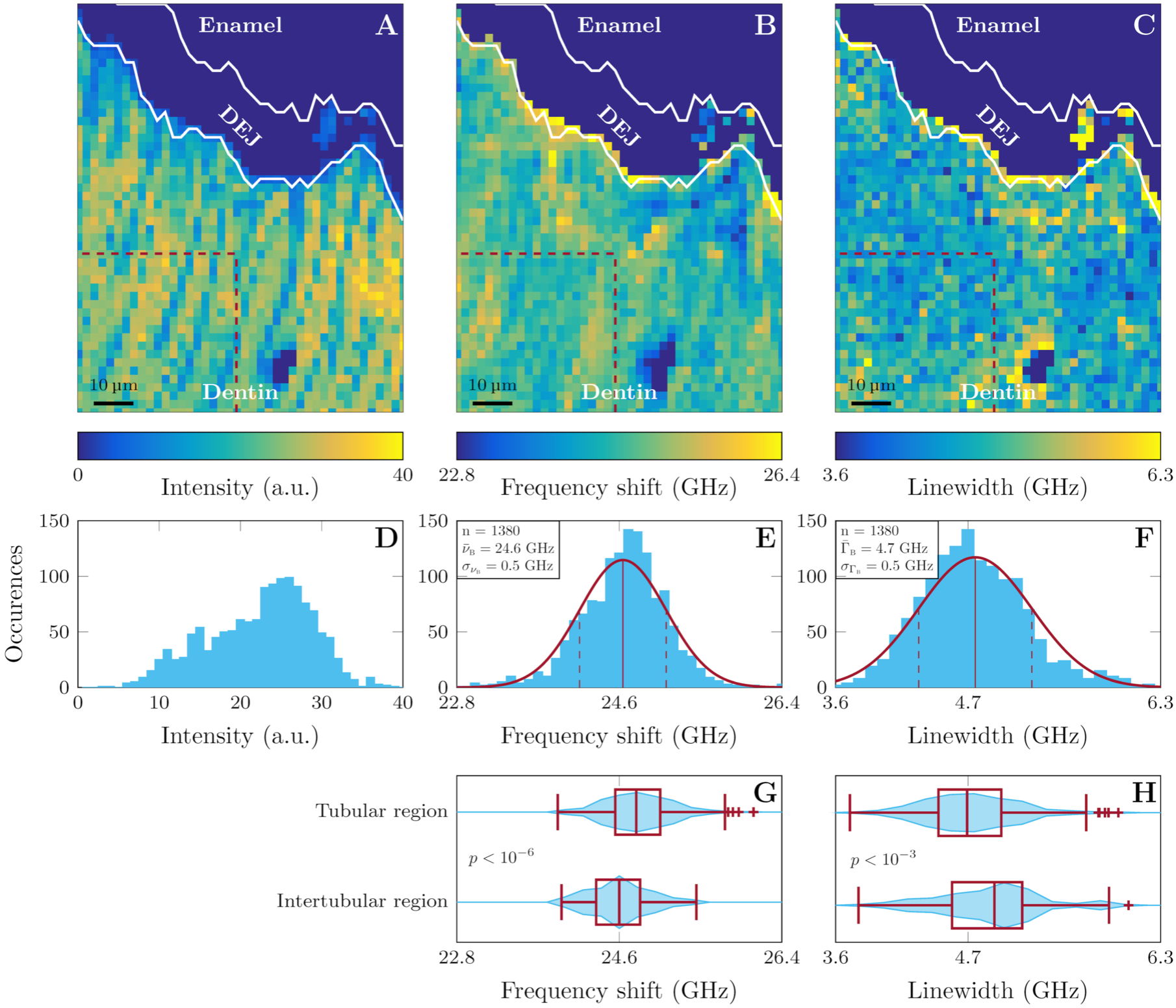
A
B
C
Enamel
DEJ
Dentin
10 µm
0
40
Intensity (a.u.)
22.8
26.4
Frequency shift (GHz)
3.6
6.3
Linewidth (GHz)
D
E
F
Occurences
150
100
50
0
10
20
30
n = 1380
$\bar{\nu}_B = 24.6$ GHz
$\sigma_{\nu_B} = 0.5$ GHz
24.6
n = 1380
$\bar{\Gamma}_B = 4.7$ GHz
$\sigma_{\Gamma_B} = 0.5$ GHz
4.7
G
H
Tubular region
Intertubular region
$p < 10^{-6}$
$p < 10^{-3}$

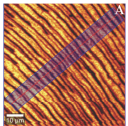

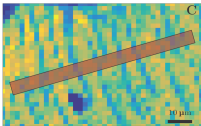

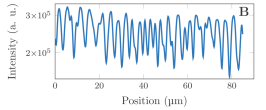

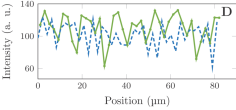

A
10 µm
C
10 µm
B
Intensity (a. u.)
3×10^5
2×10^5
0
20
40
60
80
Position (µm)
D
Intensity (a. u.)
140
100
60
0
20
40
60
80
Position (µm)

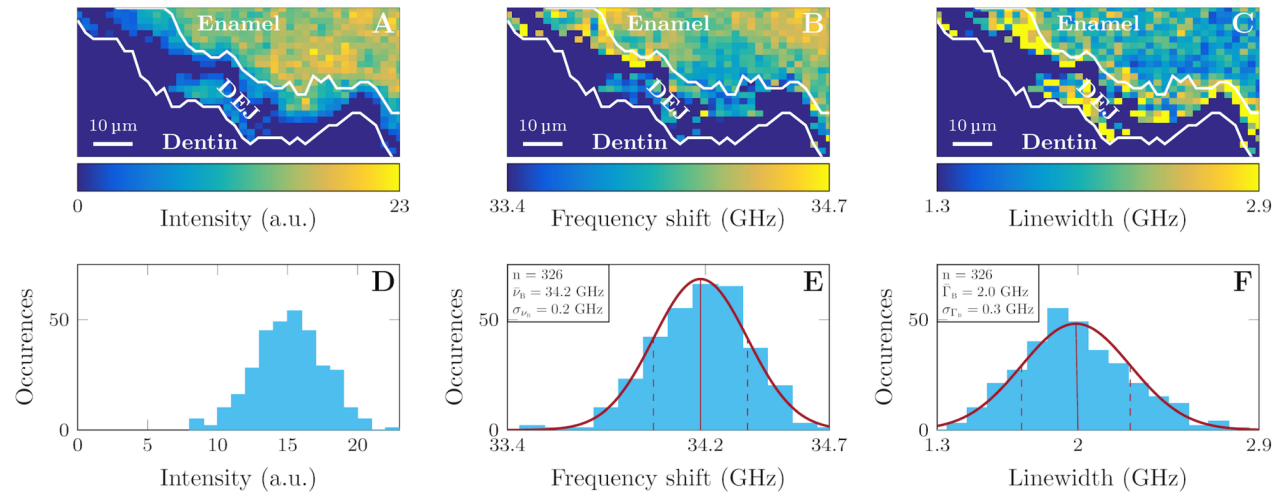
Enamel
A
DEJ
10 µm
Dentin
0
23
Intensity (a.u.)
Enamel
B
DEJ
10 µm
Dentin
33.4
34.7
Frequency shift (GHz)
Enamel
C
DEJ
10 µm
Dentin
1.3
2.9
Linewidth (GHz)
D
Occurences
50
0
0
5
10
15
20
Intensity (a.u.)
n = 326
$\bar{\nu}_B = 34.2$ GHz
$\sigma_{\nu_B} = 0.2$ GHz
E
Occurences
50
0
33.4
34.2
34.7
Frequency shift (GHz)
n = 326
$\bar{\Gamma}_B = 2.0$ GHz
$\sigma_{\Gamma_B} = 0.3$ GHz
F
Occurences
50
0
1.3
2
2.9
Linewidth (GHz)

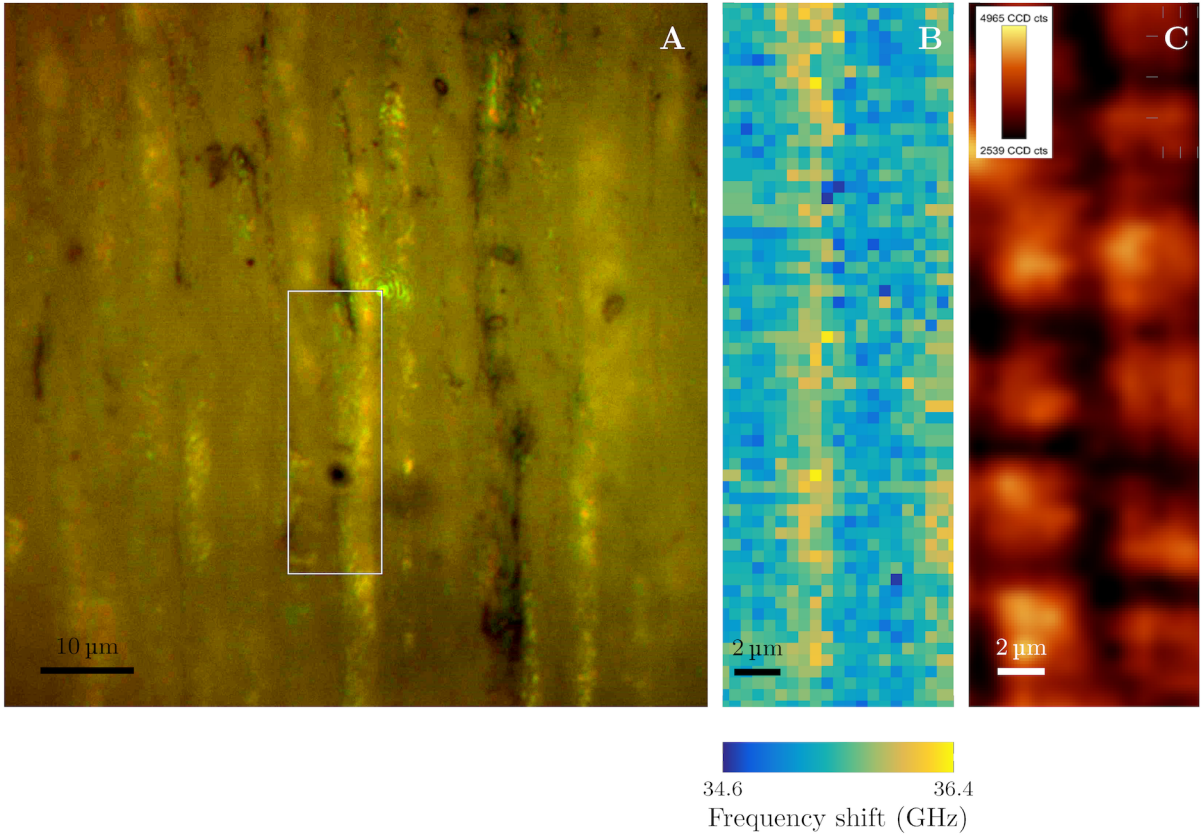
A
B
C
4965 CCD cts
2539 CCD cts
10 µm
2 µm
2 µm
34.6
36.4
Frequency shift (GHz)

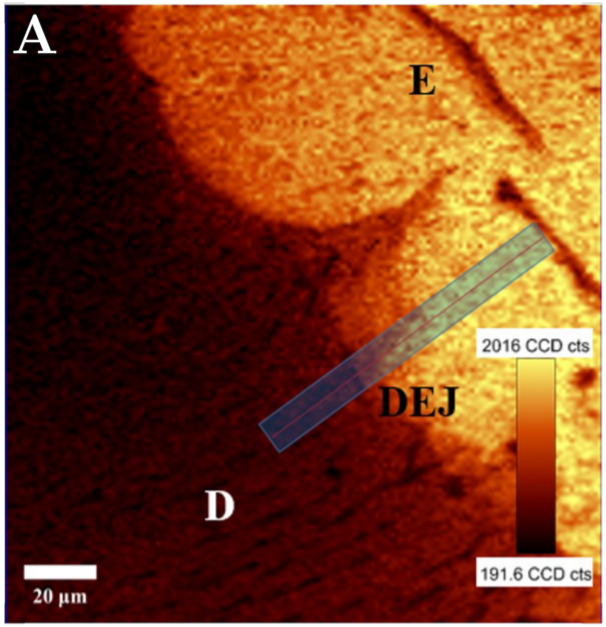
A
E
DEJ
D
2016 CCD cts
191.6 CCD cts
20 µm

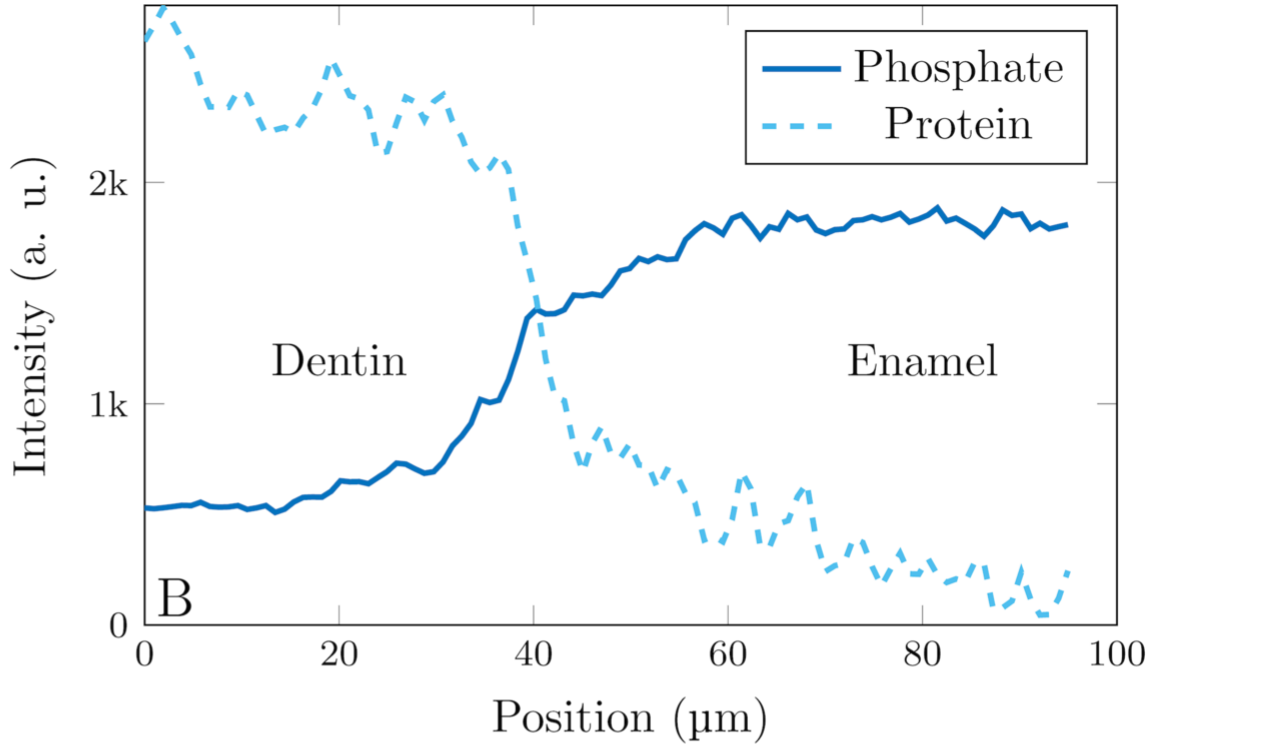
Phosphate
Protein
Intensity (a. u.)
2k
1k
0
Dentin
Enamel
B
0
20
40
60
80
100
Position (µm)

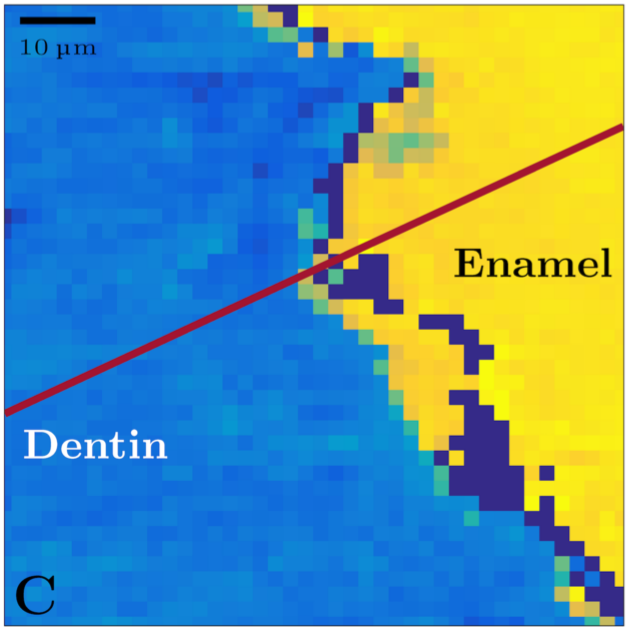
10 µm
Enamel
Dentin
C


Frequency shift (GHz)
22
35

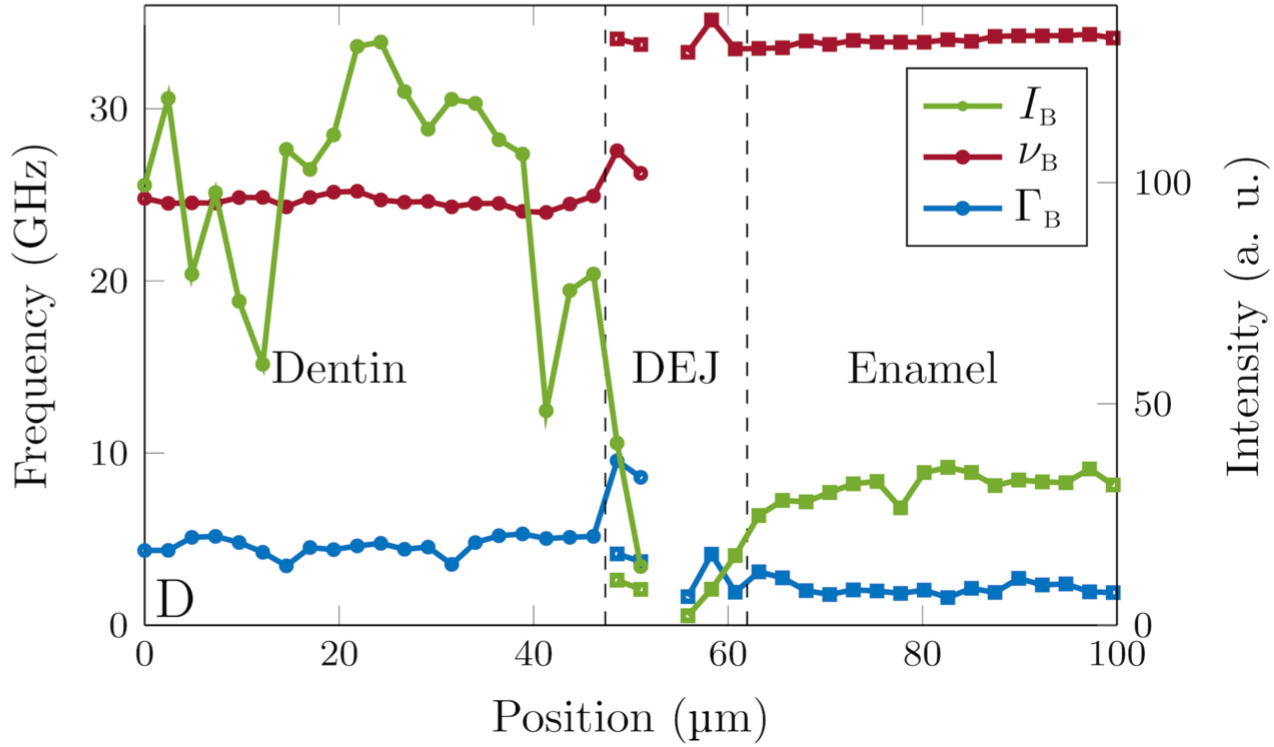
I_B
ν_B
Γ_B
Frequency (GHz)
Intensity (a. u.)
30
20
10
0
100
50
0
Dentin
DEJ
Enamel
D
0
20
40
60
80
100
Position (µm)